NANO LETTERS
Letter
Cite This: Nano Lett. XXXX, XXX, XXX−XXX
pubs.acs.org/NanoLett

Deterministic Nanoassembly of Quasi-Three-Dimensional Plasmonic Nanoarrays with Arbitrary Substrate Materials and Structures

Bongjoong Kim,[†,○] Jiyeon Jeon,[‡,○] Yue Zhang,[§,○] Dae Seung Wie,[†] Jehwan Hwang,[‡] Sang Jun Lee,[‡] Dennis E. Walker, Jr.,[∥] Don C. Abeysinghe,[⊥] Augustine Urbas,[⊥] Baoxing Xu,[*,§] Zahyun Ku,[*,⊥] and Chi Hwan Lee[*,†,#,▽]

[†]School of Mechanical Engineering, Purdue University, West Lafayette, Indiana 47907, United States
[‡]Division of Industrial Metrology, Korea Research Institute of Standards and Science, Daejeon 34113, Korea
[§]Department of Mechanical and Aerospace Engineering, University of Virginia, Charlottesville, Virginia 22903, United States
[∥]Sensors Directorate, Air Force Research Laboratory, Wright-Patterson AFB 45433, United States
[⊥]Materials and Manufacturing Directorate, Air Force Research Laboratory, Wright-Patterson AFB 45433, United States
[#]Weldon School of Biomedical Engineering, Purdue University, West Lafayette, Indiana 47907, United States
[▽]Department of Speech, Language, and Hearing Sciences, Purdue University, West Lafayette, Indiana 47907, United States

Supporting Information

ABSTRACT: Guided manipulation of light through periodic nanoarrays of three-dimensional (3D) metal−dielectric patterns provides remarkable opportunities to harness light in a way that cannot be obtained with conventional optics yet its practical implementation remains hindered by a lack of effective methodology. Here we report a novel 3D nanoassembly method that enables deterministic integration of quasi-3D plasmonic nanoarrays with a foreign substrate composed of arbitrary materials and structures. This method is versatile to arrange a variety of types of metal−dielectric composite nanoarrays in lateral and vertical configurations, providing a route to generate heterogeneous material compositions, complex device layouts, and tailored functionalities. Experimental, computational, and theoretical studies reveal the essential design features of this approach and, taken together with implementation of automated equipment, provide a technical guidance for large-scale manufacturability. Pilot assembly of specifically engineered quasi-3D plasmonic nanoarrays with a model hybrid pixel detector for deterministic enhancement of the detection performances demonstrates the utility of this method.

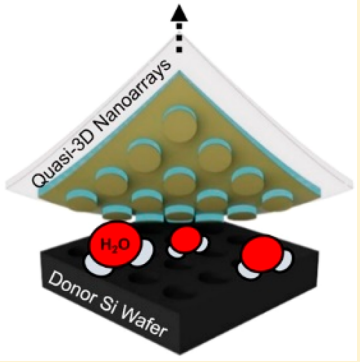

KEYWORDS: *Plasmonic film, quasi-3D nanoarrays, deterministic nanoassembly, water-assisted transfer printing method*

Interaction of incident light with three-dimensional (3D) metal−dielectric composite nanoarrays provides unique capabilities to manipulate light at nanoscale length.[1−7] Diverse types of 3D or quasi-3D plasmonic nanoarrays with tailored feature shapes, sizes, and configurations have been explored for a broad range of light-driven sensors and actuators such as imagers, biosensors, lasers, and antennas.[8−14] Traditionally, the construction of 3D plasmonic nanoarrays has largely relied on the use of nanolithography techniques by exploiting either electron-beam lithography (EBL), or focused ion-beam lithography (FIB), or interference lithography (IL), but their laborious, complex, and time-consuming nature impedes practical applications.[15−18] In addition, the nanolithography processes often require the use of thermal and chemical treatments, leading to additional increase of complexity and risk in protecting the substrate materials. Alternative strategies involve the use of micro/nanoscale 3D printing techniques such as nanoimprinting and modular microtransfer printing, allowing for deterministic integration of 3D plasmonic nanoarrays with a foreign receiver substrate, and thereby circumventing the incompatibility of the nanolithography conditions with substrate materials.[19−22] Nevertheless, the choice of receiver substrates remains limited by the required physical contact forces during printing steps, yielding an increased risk of potential damages to receiver substrates particularly composed of mechanically fragile materials and structures.

Herein, we report a new 3D nanoassembly method that enables intact separation of various types of quasi-3D plasmonic nanoarrays from their donor fabrication substrate and then transfer them to a preferred receiver substrate in a way that allows the donor substrate to be recycled for a cost- and time-saving solution. Unlike conventional approaches, the entire process of this method exclusively occurs in distilled

Received: June 26, 2019
Revised: July 24, 2019
Published: July 26, 2019

DOI: 10.1021/acs.nanolett.9b02598
Nano Lett. XXXX, XXX, XXX−XXX

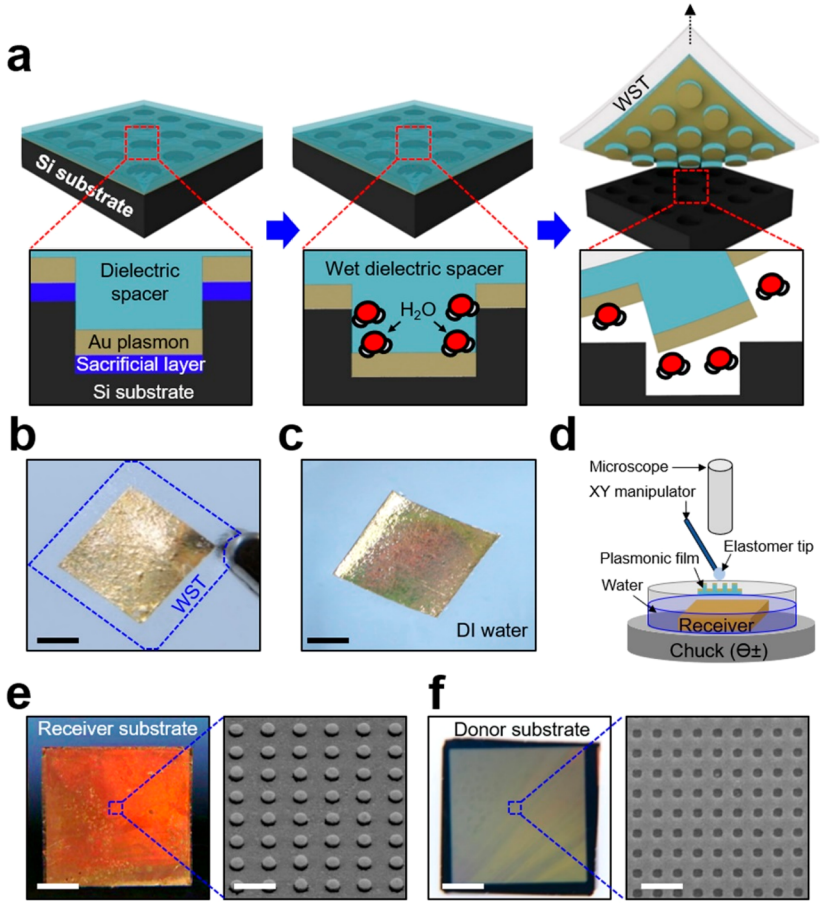

Figure 1. Three-dimensional nanoassembly method. (a) Schematic illustration for physical separation of quasi-3D plasmonic nanoarrays from its donor Si substrate. (b) Photo of a plasmonic film configured with quasi-3D nanoposts on a WST after the separation. Scale bar is 3.5 mm. (c) Photo of the plasmonic film afloat on the surface of water after dissolution of the WST. Scale bar is 3.5 mm. (d) Schematic illustration of the microscale positioning and alignment setup. (e) Photo (left) and enlarged SEM image (right) of the transferred plasmonic film on a receiver Si substrate. Scale bars are 3 mm (left) and 4 μm (right). (f) Photo (left) and enlarged SEM image (right) of the donor Si substrate. Scale bars are 3 mm (left) and 6.5 μm (right).

water under ambient conditions without the need of further chemical, thermal, or mechanical treatments, and which thereby can substantially extend the types of receiver substrate to nearly arbitrary materials and structures. Pilot assembly of specifically designed quasi-3D plasmonic nanoarrays with mid-wavelength infrared type-II superlattice (MWIR-T2SL)-based hybrid pixel detector (HPD) in a defect-free manner demonstrates the effectiveness of this method in deterministic enhancement of the detection performances. Both analytical predictions and experimental validations reveal the underlying optical and physical properties of the resulting optical systems to confirm the integrity after the assembly process.

Results and Discussion. *Three-Dimensional Nanoassembly Method.* Figure 1a shows schematic illustrations of physical separation of quasi-3D plasmonic nanoarrays from their donor Si substrate that is configured with periodic circular patterns at nanoscale. Here, these patterns are preformed on the donor Si substrate by exploiting conventional EBL,[23,24] of which representative scanning electron microscopy (SEM) images appear in Figure S1. The process begins by depositing a sacrificial Ni layer (10 nm) and Au plasmon film (50 nm) by electron-beam (e-beam) evaporator on a donor Si substrate, followed by spin-casting of a dielectric spacer using either poly(methyl methacrylate) (PMMA), benzocyclobutene (BCB), or SU-8 to form an optical cavity (Figure 1a, left). The next step involves immersing the entire structure in a bath of etchant (TFB, Transene), allowing the etchant to penetrate through the dielectric spacer[25,26] and then remove the underneath Ni layer exclusively. This allows the remaining layers to sink and adhere on the surface of the donor Si substrate by weak van der Waals adhesive force (Figure 1a, middle). The resulting structure is then rinsed with distilled water to keep the dielectric spacer wet while the top surface is wiped with a cleanroom swab to stay dry where a water-soluble tape (WST, Aquasol) is attached to serve as a temporary handling holder. Finally, mechanical peeling of the WST occurs at constant rate of 50 mm/min by using an automated tool (Mark-10), resulting in intact separation of the quasi-3D plasmonic film from the donor Si substrate (Figure 1a, right and Movie S1). Figure 1b provides an optical image of a representative specimen configured with an array (1×1 cm^2) of quasi-3D nanopost configurations, which is peeled intactly from its donor Si substrate with a WST. A subsequent placement of the WST on the surface of water leads to complete dissolution within ~10 min at room temperature, allowing the remaining quasi-3D plasmonic nanoarrays to stay afloat on the water surface (Figure 1c).

The next "assembly" step occurs by exploiting a custom-setting in which a plastic Petri dish of distilled water (~50 mL) is placed on a probe station (Signatone) where a preferred

DOI: 10.1021/acs.nanolett.9b02598
Nano Lett. XXXX, XXX, XXX−XXX

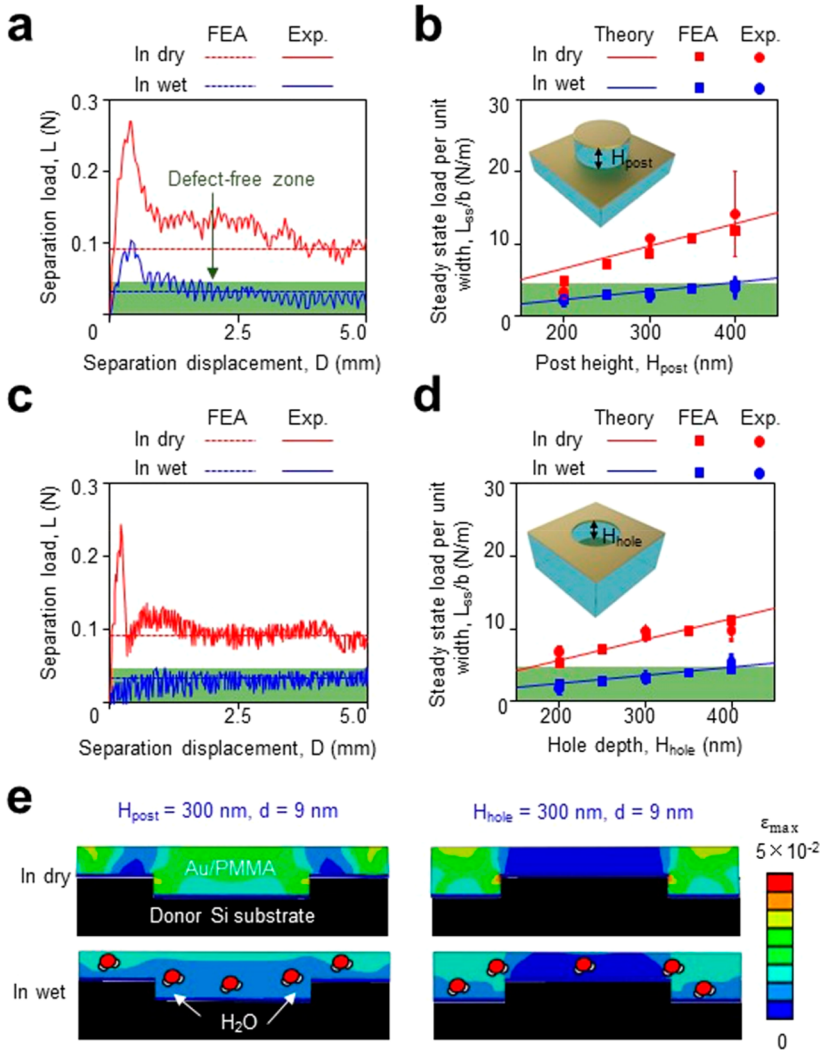

Figure 2. Mechanism study and mechanics analysis. (a) Experimental and FEA results of the separation load (L)-separation displacement (D) curves for quasi-3D plasmonic nanoposts under dry (red) and wet (blue) conditions. (b) Experimental, FEA and theoretical results for the effect of H_{post} on L_{ss}/b. (c) Experimental and FEA results of the separation load (L)-displacement (D) curves for quais-3D plasmonic nanoholes under dry (red) and wet (blue) conditions. (d) Experimental, FEA, and theoretical results for the effect of H_{hole} on L_{ss}/b (e) FEA results of strain distributions in the nanoarrays during the interfacial separation under dry and wet conditions.

receiver substrate is immersed and anchored underneath the water by a distance of <1 mm from the surface (Figure 1d). Details of this setting appear in Figure S2. Here, the quasi-3D plasmonic nanoarrays remain afloat on the water surface and can be slipped with full XY movement and 360° rotation by using a micromanipulator (Signatone) for precise positioning and alignment. Upon proper positioning, the water in the Petri dish is slowly removed, or evaporated, until the plasmonic nanoarrays reach to the surface of the receiver substrate and remain contacted via van der Waals adhesion force. Upon any misalignment, the receiver substrate is obliquely soaked in water with an angle of ∼20° from the surface,[27] allowing the misaligned plasmonic nanoarrays to be released from the receiver substrate by surface tension of water (Movie S2). Finally, the assembled structure is dried at room temperature to secure the interfacial bonding or if allowed by the receiver substrate can be annealed at ∼60 °C for 10 min in a convection oven to substantially promote the adhesion[28] by more than 50% (Figure S3). The entire process of this method is also schematically illustrated in Figure S4.

Figure 1e provides a photo (left) and a SEM image (right) of the transferred quasi-3D plasmonic film on a model foreign receiver substrate such as double-side polished (DSP) Si wafer. The results display no visual defects or damages over the area. The optical images in Figure 1f confirm the integrity of the donor Si substrate which allows its multiple recycles through postcleaning inspections and thereby can serve as a major cost- and time-saving factor (Figure S5). Comprehensive evaluations by exploiting different types of the dielectric spacer such as BCB or SU-8 produce consistent results (Figure S6).

Mechanism Study and Mechanics Analysis. The interfacial separation between quasi-3D plasmonic nanoarrays and donor Si substrate under wet (distilled water) condition occurs by overcoming the wet adhesion of confined water molecules between Au and Si, where the underneath Ni layer is completely removed. Figure 2a shows experimental and finite element analysis (FEA) results of the separation load (L)-separation displacement (D) curves, obtained with an array (1 × 1 cm^2) of quasi-3D Au (50 nm)/PMMA (1 μm)-based nanoposts under dry (red color, 20% relative humidity) and wet (blue color, distilled water) conditions. The results

DOI: 10.1021/acs.nanolett.9b02598
Nano Lett. XXXX, XXX, XXX−XXX

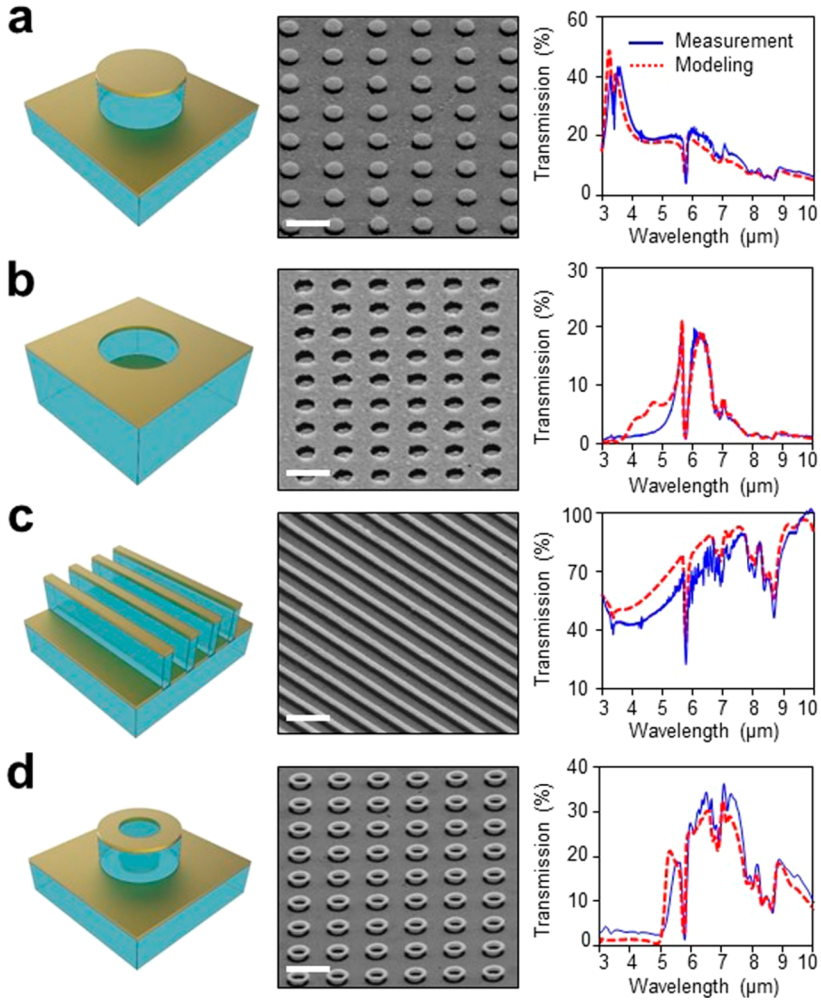

Figure 3. Demonstrations on various types of quasi-3D plasmonic nanoarrays. An arrangement of schematic illustrations (left column), SEM images (middle column), and analysis of transmission spectra (right column) for a range of quasi-3D plasmonic nanoarrays configured with (a) nanoposts, (b) nanoholes, (c) bilayer nanowire gratings, and (d) ring-shaped disks. Scale bars are 3.3, 2.0, 1.8, and 2.0 μm from the top.

produce consistent agreements in which the L increases rapidly at the edge within ~1 mm of the specimen, and then decreases until it becomes constant to the steady state (L_{ss}). Notably, a substantial decrease of the L_{ss}, by more than ~70%, occurs under the wet condition as compared with that under the dry condition. These results indicate that the presence of water molecules indeed results in the reduction of interfacial energy at the 3D nanoscale featured surface. The green-filled area in Figure 2a defines a defect-free zone where the separated plasmonic nanoarrays remain intact with the successful yield of nearly 100% (among >100 testbed specimens). A representative image of the damaged specimen when the L_{ss} is peeled out of the defect-free zone appears in Figure S7. The defects may also occur due to any potential residues of the underneath Ni layer, consequently resulting in the increase of the L_{ss}.

Figure 2b shows experimental, computational (FEA), and theoretical results that reveal the effect of the nanopost height, H_{post} (inset), on L_{ss}. The results indicate that the steady state separation load per unit width (L_{ss}/b) of the specimen is increased as the H_{post} is increased from 200 to 400 nm, which is attributed to the increased deformation energy required for longer nanoposts. In theory, the energy balance of quasistatic interfacial separation can be expressed as[29] $W_L = W_{interface} + W_{deformation}$, where W_L ($= L_{ss} \times \Delta D$) is the work done by the L_{ss} and ΔD is the separation displacement; $W_{interface}$ ($= G \times b \times \Delta D$) is the interfacial adhesion energy between the plasmonic nanoarrays and the donor Si substrate, where G is the adhesion energy per unit area at the interface; $W_{deformation}$ ($= u \times b \times \Delta D \times H_{post}$) is the deformation energy of the quasi-3D nanoposts, where u is the deformation energy density. As a consequence, the energy balance leads to $L_{ss}/b = G + u \times H_{post}$, wherein the G and u are independent of the H_{post} because both the interface and materials properties of the quasi-3D nanoposts remain unchanged. These assessments are consistent with the experimental observations that the L_{ss} under wet condition is substantially smaller than that under dry condition for the same H_{post}, mainly due to the reduced interfacial adhesion energy by the effect of water molecules. The control evaluations by exploiting a similar quasi-3D plasmonic nanoarrays with a nanohole configuration (Figure 2c and d) produce consistent results to support and confirm these findings.

Figure 2e provides the corresponding modeling (FEA) results that reveal the underlying strain distributions of the plasmonic nanoarrays during the interfacial separation process under the dry (top row) and wet conditions (bottom row). Here, the modeled structure includes a unit of Au (50 nm)/PMMA (1 μm) composites configured with quasi-3D nano-

DOI: 10.1021/acs.nanolett.9b02598
Nano Lett. XXXX, XXX, XXX−XXX

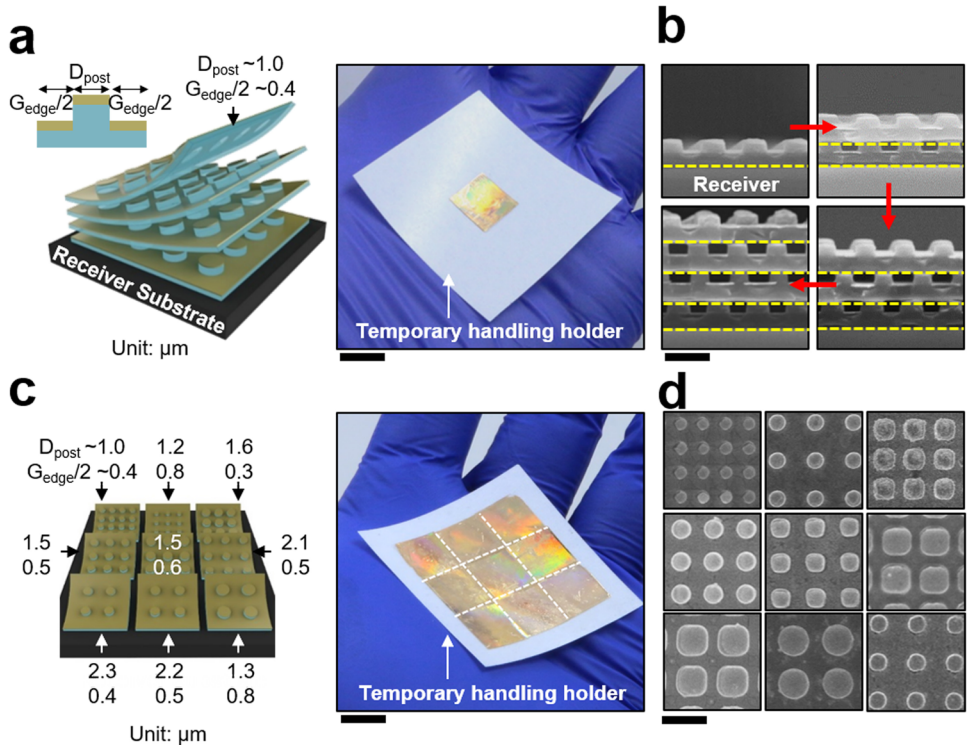

Figure 4. Heterogeneous modular assembly with controlled spatial arrangements. (a) Schematic illustration (left) and photo (right) of multiple stacked plasmonic nanoarrays configured with identical quasi-3D nanoposts. Scale bar is 1 cm. (b) The enlarged SEM images of the first, second, third, and fourth layer-stacked nanoposts. Scale bar is 2.3 μm. (c) Schematic illustration (left) and photo (right) of a 3 × 3 array of dissimilar quasi-3D plasmonic nanoposts featured with different sizes and arrangements. Scale bar is 1 cm. (d) The enlarged SEM images of the each transferred module. Scale bar is 3.3 μm.

posts (left column, H_{post} = 300 nm) and nanoholes (right column, H_{hole} = 300 nm), where d is defined as the distance between the separated plasmonic nanoarrays and the donor Si substrate (Figure S8). The results reveal that the maximum principal strain (ε_{max}) appears in the PMMA layer where the magnitude in wet condition is >60% smaller than that in dry condition. This aspect allows the Au film to experience insignificant mechanical constraints during the interfacial separation process and thereby can reduce the potential risk of defects, which is consistent with the above-mentioned experimental observations. The corresponding modeling results for varied d, H_{post}, and H_{hole} as well as by exploiting different dielectric spacers (BCB or SU-8) under both dry and wet conditions are summarized in Figures S9−S12. Details of the modeling appear in Materials and Methods.

Applicability to Diverse Types of Quasi-3D Plasmonic Nanoarrays. This 3D nanoassembly method is applicable to diverse types of quasi-3D metal−dielectric composite nanoarrays. Figure 3 presents an arrangement of schematic illustrations (left column), SEM images (middle column), and transmission spectra measurements (right column) for a range of quasi-3D plasmonic nanoarrays configured with (a) nanoposts, (b) nanoholes, (c) bilayer nanowire gratings, and (d) ring-shaped disks, each of which is transferred from its donor Si substrate to a foreign DSP Si wafer. Detailed geometric information for these plasmonic nanoarrays appears in Figure S13 with the minimum width of the nanoarrays ranging from 250 nm to 1.5 μm. The collective set of the SEM images indicates that no visual defects appear along the surface of the transferred nanoarrays regardless of the feature sizes, shapes, and configurations. In addition, the continued agreement between the transmission spectra of experimental (blue color) and modeling (red color) results support these observations, each of which is obtained using the Fourier transform infrared (FTIR) spectrometer (Nicolet 5700) and the Computer Simulation Technology (CST) Microwave Studio based on the finite integration technique (FIT), respectively. Repetitive transmission measurements of the specimens at widely spread locations produce consistent outcomes (Figure S14), highlighting the uniformity and integrity over the area (1 × 1 cm^2).

Heterogeneous Modular Assembly with Controlled Spatial Arrangement. The ability to assemble several identical or different types of quasi-3D plasmonic nanoarrays in a spatially controlled manner provides a mean of attaining advanced light manipulation.[30−35] Figure 4a shows a schematic illustration (left) and a photo (right) of multiple stacked plasmonic films configured with identical quasi-3D nanoposts in which each unit is sequentially transferred from its donor Si substrate to a single DSP wafer loaded on a temporary handling holder. The adhesion at the interface between each transferred plasmonic film can be secured by post-annealing treatment in a convention oven at 60 °C for 10 min. Here, the transferred nanoposts exhibit the diameter (D_{post}) of 1.0 μm and the edge-to-edge gap (G_{edge}) of 800 nm (inset schematic). The enlarged SEM images of the first (left top), second (right top), third (right bottom), and fourth (left bottom) layer-stacked nanoposts (Figure 4b) and the corresponding results of transmission spectra measurements (Figure S15) consistently indicate that no defect occurs throughout the multiple stacking process. The relative alignment error of each stacked layer remains below 1 μm, which can be furthermore improved

DOI: 10.1021/acs.nanolett.9b02598
Nano Lett. XXXX, XXX, XXX−XXX

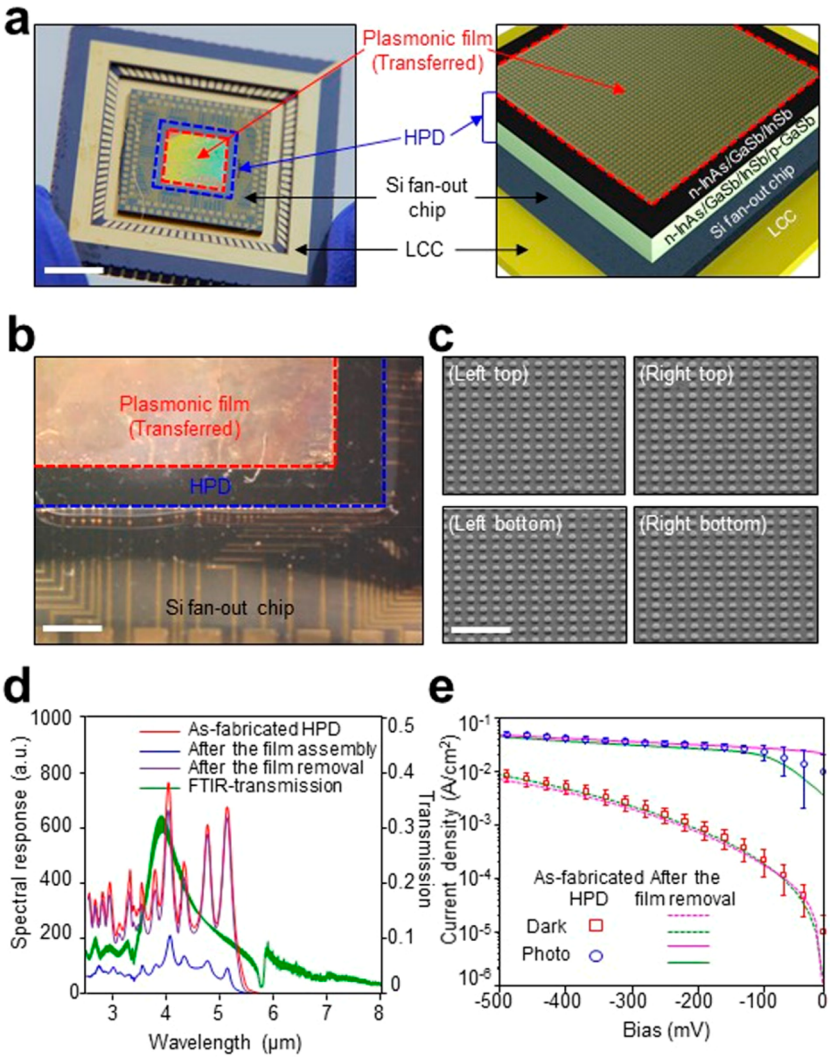

Figure 5. Pilot assembly and post electro-optical (EO) analysis. (a) Photo (left) and schematic illustration (right) of a demonstration system. Scale bar is 4.5 mm. (b) Microscope image of the demonstration system. Scale bar is 1.0 mm. (c) The enlarged SEM images taken from widely spread locations on the surface of transferred nanoposts. Scale bar is 10 μm. (d) EO-measured spectral HPD-responses and FTIR-measured transmission of the specimens. (e) Measured dark- and photocurrents of the specimens.

by employing alignment marks. Figure 4c presents another experimental demonstration that involves multiple modular assemblies to construct a larger array of dissimilar quasi-3D plasmonic nanoposts that exhibit different sizes (D_{post} = 1.0−2.3 μm) and arrangements (G_{edge} = 0.6−1.6 μm). The enlarged SEM images of the each transferred module (Figure 4d) and the corresponding results of transmission spectra measurements (Figure S16) provide continued consistency. These demonstrations highlight the reliability and repeatability of this method, which is highly desired for many envisioned plasmonic applications.

Pilot Assembly and Post Electro-Optical (EO) Analysis. Pilot assembly of quasi-3D plasmonic nanoarrays with a sophisticatedly designed HPD illustrates the feasibility and utility of this method in the deterministic manipulation of light spectrum in order to enhance the detection performances and functionalities beyond its standards.[36−40] Figure 5a presents a photo (left) and a schematic illustration (right) of the demonstrative system. Here, a MWIR-T2SL-based HPD serves as a model receiver system, of which the basic components include GaSb (p-type) for top contact (300 nm), InAs/GaSb/InSb for active (×300 periods, 1.9 μm)/bottom (×80 periods, 508 nm) superlattice and indium (In) bumps for connections, all assembled in a flip-chip-on-laminate configuration (Figure S17).[36] The constituent materials and structures of this model receiver system represents a chemically and mechanically vulnerable receiver substrate that is otherwise difficult to directly construct such quasi-3D plasmonic nanoarrays by using conventional nanolithography or micro/nanoscale printing techniques. The process begins by mounting the HPD on a leadless chip carrier (LCC) to serve as a temporary handling holder that allows the HPD to avoid any physical contact during the entire process. The resulting structure is then immersed underneath distilled water in a Petri dish while a unit (1 × 1 cm^2) of quasi-3D Au (50 nm)/PMMA (800 nm) nanoposts (H_{post} = 0.2 μm, D_{post} = 1 μm, G_{edge} = 1 μm) stays afloat on the water surface. The subsequent assembly step takes place on the probe station with full *XY* movements and 360° rotation under microscope examinations (Movie S3). Drying of the assembled unit at room-temperature finishes the process. A representative microscope image of the complete system (Figure 5b) suggests that the receiver HPD is in its

DOI: 10.1021/acs.nanolett.9b02598
Nano Lett. XXXX, XXX, XXX−XXX

integrity with no visible defects or damages along the surface. The enlarged SEM images taken from widely spread locations on the surface of the transferred nanoposts support these observations (Figure 5c).

The post electro-optical (EO) analysis takes place in a custom measurement setup that allows for the acquisition of optical-to-electrical-measured spectral responses at 77 K (Figure S18). Figure 5d presents representative measurement results obtained with the following specimens; (a) the as-fabricated HPD (red color), (b) the HPD after assembly of the nanoposts (blue color), and (c) the HPD after removal of the nanoposts (purple color) by acetone to dissolve the underneath PMMA layer and thereby strip the entire Au plasmon film (Figure S19). The inset graph (green color) shows the corresponding FTIR-measured transmission after the assembly process. The results indicate that deterministic adjustment of the waveguide resonance occurs in the HPD after the assembly (blue color) in which distinct oscillatory characteristics appear in all of the spectral responses due to the Fabry−Perot cavity resonances between air and the embedded mirror planes consisting of ohmic contact under bump metallization and In bump.[41−43] The transmitted light through the narrow gaps of the nanoposts exhibits waveguide resonance behavior that is correlated to interactions between the embedded Au plasmonic layers where the maximum value of the electric field magnitude ($|E|$) occurs at the peak wavelength.[44,45] The corresponding FIT-simulated $|E|$ distribution at the peak wavelength appears in Figure S20. Importantly, the spectral responses after removal of the nanoposts remain barely changed from those of the as-fabricated HPD within the range of measurement error, providing clear evidence of retaining intact even after the assembly and removal of the nanoposts. Figure 5e provides quantitatively comparable results of dark- and photocurrents between the as-fabricated HPD (symbols) and after the removal of the nanoposts (lines) at the applied bias voltage ranging from −500 mV to 0 V, all obtained using a custom measurement setup at 77 K (Figure S21). The results show that the dark- and photocurrents undergo negligible changes within the range of measurement error, which consistently implies that the intrinsic performances of the receiver HPD remain preserved without any degradation in the performance.

Conclusion. The results outlined herein illustrate a novel 3D nanoassembly method that occurs under wet condition, enabling intact integration of various quasi-3D plasmonic nanoarrays with a desired foreign substrate. Uniquely, the entire process of this method requires no chemical and thermal treatments (except water at room temperature) and physical contact forces (except weak van der Waals contact force) and thereby leads to a large extension of the types of receiver substrate to nearly arbitrary materials and structures. This method provides both reliability and repeatability, allowing for the construction of various types of quasi-3D plasmonic nanoarrays on preferred receiver substrates with the successful yield of nearly 100% (among >100 testbed specimens) in a defect-free manner that allows the donor substrates to be recycled multiple times. The comprehensive set of data gained from both experimental, computational, and theoretical studies provides an insight into fundamental principles and design trade-offs for identifying optimal conditions for the defect-free outcomes. The advanced features of multiple modular assemblies in lateral and vertical configurations, taken together with the implementation of a set of automated equipment for precisely controlled assembly protocols, suggest the controllability and modular scalability of this method. The constituent quasi-3D composite materials and structures presented in this report are not the only options that can be achieved by this method, and broader considerations of even more complex or further downscaled 3D nanoarchitectures[46−48] and nanoelectronics[49−51] suggest directions for future research.

Materials and Methods. *Fabrication of Donor Si Substrates.* Conventional EBL technique was used to produce various periodic nanopatterns of a photoresist layer on a Si substrate. A thin layer (20 nm) of Cr formed by e-beam evaporator was used to serve as a selective masking layer for subsequent etching of Si. A brief isotropic etching with CF_4/O_2 (13/2 sccm; 45 mTorr; 100 W) for 10 min was followed to slightly taper the sidewall of the Si patterns by ∼80° from the ground (Figure S22) in order to serve a passage for solutions (distilled water or etching solutions) to more easily pass through the dielectric spacer. Finally, the Cr masking layer was removed by immersing in a bath of a Cr etchant for ∼30 s to complete the entire process.

Computational Analysis. The FEA was performed by using the ABAQUS/standard package. The material deformation of the PMMA was modeled by viscoelastic−plastic behavior with the mechanical modulus (E) and the Poisson's ratio (ν) E = 3.0 GPa and ν = 0.35, and yield stress σ_y = 40 MPa. The plasmon Au film was modeled by elastic-perfectly plastic behavior with E = 79 GPa, ν = 0.42 and yield stress σ_y = 200 MPa. The donor Si substrate was modeled by linear elastic model with E = 130 GPa and ν = 0.27. A mesh convergence study was conducted in advance to confirm the discretization of model sufficiently enough for extracting converged separation force. The interfacial separation between the plasmon Au film and the donor Si substrate was modeled using the cohesive zone model with a bilinear traction−separation relation. In the cohesive zone model, the interfacial traction−separation relation was characterized by the following two key parameters: (1) cohesive strength (σ_0, the maximum traction in the traction-separation curve), and (2) fracture toughness (Γ_c, the area of the traction−separation curve). In this study, the cohesive strength of σ_0 = 31 and 13 MPa and the fracture toughness of Γ_c = 0.48 and 0.19 J/m^2 were used for the dry and wet conditions, respectively.[29,52] A constant displacement loading rate was applied on the top to delaminate quasi-3D plasmonic nanoarrays while the donor Si substrate was fixed.

Numerical Simulation of Transmission. Numerical simulation was conducted by using the CST Microwave Studio-based on a finite integration technique (FIT) to design various quasi-3D plasmonic nanoarrays and to understand their underlying mechanisms such as localized surface plasmon (SP), propagating SP, waveguide resonance mode, and the Fabry−Perot resonance. In the CST simulator, a single unit cell was simulated with appropriate boundary conditions including the transverse magnetic field equal to zero (perfect magnetic conductor, PMC) and the transverse electric field equal to zero (perfect electric conductor, PEC), and a TEM plane wave was simulated to propagate in the z-direction. The direction of polarized incoming light was parallel to the x-axis, as also illustrated in Figure S14. The refractive index of PMMA and the permittivity of Au used in these simulations were measured by spectroscopic ellipsometry (Figure S23). The wavelength-independent refractive index of the DSP Si wafer, n_{Si} = 3.4, was used.

DOI: 10.1021/acs.nanolett.9b02598
Nano Lett. XXXX, XXX, XXX−XXX

FTIR Measurements. The transmission spectra were recorded by the Nicolet 5700 Fourier transform infrared (FTIR) spectrometer with a liquid nitrogen-cooled mercury−cadmium−telluride detector and KBr beam splitter in the wavelength range of 3−10 μm.

Fabrication of MWIR-T2SL-based HPD. For the fabrication of the MWIR-T2SL, InAs/GaSb type-II superlattice (SL) device structure was grown on a 2 in. n-type GaSb substrate with a solid source molecular beam epitaxy (MBE) machine. A 300 nm GaSb buffer layer was grown to smooth the surface before the device layer growth. A 200 nm InAsSb etch stop layer was grown, followed by n-type bottom contact SL-layer (×80 periods) and absorber SL-layer (×300 periods) consisting of 10 monolayers (ML) of InAs/10 ML of GaSb/1 ML of InSb and a 300 nm p-type GaSb top contact layer. The fabrication scheme of the HPD was composed of a dry etch to form the mesa, surface passivation, ohmic metal evaporation under bump metallization, In deposition, and In reflow process. An array mesa was formed using standard photolithography, inductively coupled plasma (ICP) etching by BCl3 gas, followed by wet-chemical etching in the mixed solution of $H_3PO_4/H_2O_2/H_2O$ = 1:2:20 in order to reduce the charge density on ICP-etched mesa sidewall surfaces (surface leakage). A 200 nm thick SiO_2 was deposited for surface passivation using plasma-enhanced chemical vapor deposition (PECVD). After making it through the SiO_2, the ohmic contact metals under bump metallization and In bump were deposited by e-beam evaporation and then the deposited In was reflowed to form In bumps. The fabricated pixel array device was hybridized with a Si fan-out chip through a standard flip-chip-on-laminate process, then an underfill epoxy was injected for mechanical support between the pixel array device and the Si fan-out chip. Finally, the substrate was removed by using a series of the chemical−mechanical polishing (CMP) and selective etching to InAsSb etch stop layer. A schematic illustration of the entire fabrication procedures appears in Figure S24.

Characterization of MWIR-T2SL-Based HPD. The MWIR-T2SL-based HPD was mounted and wire-bonded to a leadless chip (LCC). The HPD was then characterized using custom-settings configured for spectral response and dark- and photocurrents. The dark current was measured in a variable temperature cryostat with a cold shield in front of the device and coldfinger cooling the device from the backside, and the photocurrent was tested using a calibrated blackbody source (900 K). The FTIR-spectrometer (Nicolet 5700) was used to spectrally evaluate the device-response over the relevant range of operating temperatures and bias voltages.

Transmission Spectra Analysis. Both arrays of the quasi-3D nanoposts and nanoholes were conceptually considered as two separate plasmonic layers of metallic disk array (MDA) and metallic hole array (MHA) on top of the PMMA spacer. The waveguide (WG) resonance mode through the nanoscale gaps in the nanoposts and nanoholes arrays was ascribed to the interaction between MDA and MHA layers, resulting in greatly enhancing the transmission (EOT, extraordinary optical transmission) and realizing easy-to-control optical filter. These arrays were designed for potential candidates of sensing techniques, termed algorithmic spectrometry wherein suitable spectral shapes of the sensor's responsivities would be achieved through the deterministic integration of nanoarrays with preexisting EO-sensors for the synthesis of a desired spectral filter shapes. The bilayer metallic nanowire gratings were designed for the polarization of light by transmitting only a specific polarization state (p-polarized, perpendicular polarization to the nanowires), providing advantages of lowering the s-polarized (parallel polarization to the nanowires) transmission by using two self-aligned metal gratings, as compared with the traditional one-dimensional metallic grating (planar grating layer), and increasing the p-polarized transmission due to the Fabry−Perot cavity resonance in the dielectric spacer. The extinction ratio of the bilayer nanowire gratings was ∼15 dB at 7.55 μm with a high p-polarized transmission, 89%, as also seen in Figure 3 (distinct dips at ∼3.4, ∼5.8, ∼7, and 8−9 μm which were attributed to the PMMA absorptions; more specifically to the C−H bond stretching vibrations, the presence of the acrylate carboxyl group, the bending vibration of the C—H bonds, and C—O—C stretching vibration, respectively). Lastly, the ring-shaped disks were designed to isolate a wide spectral band and exhibit a high peak transmission in the passband.

■ ASSOCIATED CONTENT

Supporting Information

The Supporting Information is available free of charge on the ACS Publications website at DOI: 10.1021/acs.nanolett.9b02598.

SEM images of various nanopatterns on donor Si substrate (Figure S1); schematic and photo of the microscale positioning and alignment setup (Figure S2); measured interfacial adhesion between the transferred plasmonic nanoarrays and a receiver after curing at room temperature and postannealing (Figure S3); schematic for the entire process of the 3D nanoassembly method (Figure S4); photos of a donor Si substrate through four times recycles (Figure S5); SEM images of the transferred quasi-3D nanoposts consisted of BCB or SU-8 as a dielectric spacer (Figure S6); photo and SEM image of the defects and cracks on a specimen when peeled by the L_{ss} out of defect-free zone (Figure S7); schematic of the modeled structure (Figure S8); FEA results for quasi-3D nanoposts and nanoholes in various conditions. (Figures S9−12); detailed geometric information for the quasi-3D nanoarrays (Figure S13); repeatedly measured transmission spectra at widely spread locations of the transferred nanoarrays (Figure S14); measured transmission spectra of the 2nd, 3rd and 4th layer-stacked nanoposts (Figure S15); measured transmission spectra of the transferred each module unit (Figure S16); schematics of the model MWIR-T2SL-based HPD assembled in a flip-chip-on-laminate configuration (Figure S17); schematic diagram of a custom setup for the measurement of optical-to-electrical (EO)-measured spectral response (Figure S18); photos of the as-fabricated HPD, the HPD after the assembly of the nanoposts, and the HPD after the removal of the (Figure S19); FIT-simulated distribution of electric field magnitude (|E|) at the peak wavelength for a nanopost unit cell (Figure S20); schematic diagram of a custom setup for the measurement of dark- and photocurrent (Figure S21); schematic and SEM image of the nanohole patterns tapered by ∼80° from the ground. (Figure S22); measured complex refractive index of PMMA and Au permittivity (Figure S23);

DOI: 10.1021/acs.nanolett.9b02598
Nano Lett. XXXX, XXX, XXX−XXX

schematic illustration of the entire process for the fabrication of the HPD (Figure S24) (PDF)

The separation process of a plasmonic film configured with quasi-3D nanoposts (AVI)

Repetitive loading and unloading of a plasmonic film to/from a receiver Si substrate (MP4)

Positioning and alignment of a plasmonic film on the surface of water under microscope examination (AVI)

AUTHOR INFORMATION

Corresponding Authors

*E-mail: lee2270@purdue.edu (C.H.L.).
*E-mail: zahyun.ku.1.ctr@us.af.mil (Z.K.).
*E-mail: bx4c@virginia.edu (B.X.).

ORCID

Bongjoong Kim: 0000-0002-9969-6954
Baoxing Xu: 0000-0002-2591-8737
Chi Hwan Lee: 0000-0002-4868-7054

Author Contributions

○B.K., J.J., and Y.Z. contributed equally to this work.

Notes

The authors declare no competing financial interest.

ACKNOWLEDGMENTS

This work was supported by grants from the Air Force Research Laboratory (#S-114-054-002) and the Purdue Research Foundation (PRF). The AFRL portion of this work was supported by the AOARD Grant FA2386-18-1-4104 funded by the U.S. government (AFOSR/AOARD). The KRISS portion of this work was supported by the Nano-Material Fundamental Technology Development Program (2018069993) through the National Research Foundation of Korea (NRF) funded by Ministry of Science and ICT, the KRISS Grant GP2019-0015-03, and the AOARD Grant FA2386-14-1-4094 funded by the U.S. government (AFOSR/AOARD). The mechanics model and computations of this work were supported by the NSF-CMMI-1728149.

REFERENCES

(1) Stockman, M. I.; Kneipp, K.; Bozhevolnyi, S. I.; Saha, S.; Dutta, A.; Ndukaife, J.; Kinsey, N.; Reddy, H.; Guler, U.; Shalaev, V. M.; Boltasseva, A.; Gholipour, B.; Krishnamoorthy, H. N. S.; MacDonald, K. F.; Soci, C.; Zheludev, N. I.; Savinov, V.; Singh, R.; Gross, P.; Lienau, C.; Vadai, M.; Solomon, M. L.; Barton, D. R.; Lawrence, M.; Dionne, J. A.; Boriskina, S. V.; Esteban, R.; Aizpurua, J.; Zhang, X.; Yang, S.; Wang, D. Q.; Wang, W. J.; Odom, T. W.; Accanto, N.; de Roque, P. M.; Hancu, I. M.; Piatkowski, L.; van Hulst, N. F.; Kling, M. F. *J. Opt.* **2018**, *20* (4), 043001.

(2) Yang, X. D.; Yao, J.; Rho, J.; Yin, X. B.; Zhang, X. *Nat. Photonics* **2012**, *6* (7), 450−454.

(3) Zhang, X.; Liu, Z. W. *Nat. Mater.* **2008**, *7* (6), 435−441.

(4) Cheben, P.; Halir, R.; Schmid, J. H.; Atwater, H. A.; Smith, D. R. *Nature* **2018**, *560* (7720), 565−572.

(5) Soukoulis, C. M.; Wegener, M. *Science* **2010**, *330* (6011), 1633−1634.

(6) Atwater, H. A.; Polman, A. *Nat. Mater.* **2010**, *9* (3), 205−213.

(7) Naldoni, A.; Shalaev, V. M.; Brongersma, M. L. *Science* **2017**, *356* (6341), 908−909.

(8) Franklin, D.; Frank, R.; Wu, S. T.; Chanda, D. *Nat. Commun.* **2017**, *8*, 15209.

(9) Ni, X. J.; Wong, Z. J.; Mrejen, M.; Wang, Y.; Zhang, X. *Science* **2015**, *349* (6254), 1310−1314.

(10) Stewart, M. E.; Mack, N. H.; Malyarchuk, V.; Soares, J.; Lee, T. W.; Gray, S. K.; Nuzzo, R. G.; Rogers, J. A. *Proc. Natl. Acad. Sci. U. S. A.* **2006**, *103* (46), 17143−17148.

(11) Safaei, A.; Modak, S.; Lee, J.; Chandra, S.; Franklin, D.; Vazquez-Guardado, A.; Chanda, D. *Opt. Express* **2018**, *26* (25), 32931−32940.

(12) Vazquez-Guardado, A.; Smith, A.; Wilson, W.; Ortega, J.; Perez, J. M.; Chanda, D. *Opt. Express* **2016**, *24* (22), 25785−25796.

(13) Huang, Q. L.; Peh, J.; Hergenrother, P. J.; Cunningham, B. T. *Appl. Phys. Lett.* **2016**, *109* (7), 071103.

(14) Zhang, M.; Lu, M.; Ge, C.; Cunningham, B. T. *Opt. Express* **2014**, *22* (17), 20347−20357.

(15) Jang, W. Y.; Ku, Z.; Jeon, J.; Kim, J. O.; Lee, S. J.; Park, J.; Noyola, M. J.; Urbas, A. *Sci. Rep.* **2016**, *6*, 34876.

(16) Wang, Y.; Du, Z. D.; Park, Y. S.; Chen, C.; Zhang, X.; Pan, L. *Opt. Lett.* **2015**, *40* (16), 3918−3921.

(17) Luo, Y.; Jiang, X. X.; Liu, L.; Si, G. Y. *Nanosci. Nanotechnol. Lett.* **2018**, *10* (1), 1−12.

(18) Xia, D. Y.; Ku, Z. Y.; Lee, S. C.; Brueck, S. R. J. *Adv. Mater.* **2011**, *23* (2), 147−179.

(19) Gao, L.; Shigeta, K.; Vazquez-Guardado, A.; Progler, C. J.; Bogart, G. R.; Rogers, J. A.; Chanda, D. *ACS Nano* **2014**, *8* (6), 5535−5542.

(20) Chanda, D.; Shigeta, K.; Gupta, S.; Cain, T.; Carlson, A.; Mihi, A.; Baca, A. J.; Bogart, G. R.; Braun, P.; Rogers, J. A. *Nat. Nanotechnol.* **2011**, *6* (7), 402−407.

(21) Chanda, D.; Shigeta, K.; Truong, T.; Lui, E.; Mihi, A.; Schulmerich, M.; Braun, P. V.; Bhargava, R.; Rogers, J. A. *Nat. Commun.* **2011**, *2*, 479.

(22) Lee, S.; Kang, B.; Keum, H.; Ahmed, N.; Rogers, J. A.; Ferreira, P. M.; Kim, S.; Min, B. *Sci. Rep.* **2016**, *6*, 27621.

(23) Chen, Y. F. *Microelectron. Eng.* **2015**, *135*, 57−72.

(24) Vieu, C.; Carcenac, F.; Pepin, A.; Chen, Y.; Mejias, M.; Lebib, A.; Manin-Ferlazzo, L.; Couraud, L.; Launois, H. *Appl. Surf. Sci.* **2000**, *164*, 111−117.

(25) Kusy, R. P.; Whitley, J. Q.; Kalachandra, S. *Polymer* **2001**, *42* (6), 2585−2595.

(26) Ayme, J. C.; Emery, J.; Lavielle, L.; Lischetti, G.; Schultz, J. *J. Mater. Sci.: Mater. Med.* **1992**, *3* (5), 387−390.

(27) Cheng, C.; Shiu, K.; Li, N.; Han, S.; Shi, L.; Sadana, D. *Nat. Commun.* **2013**, *4*, 1577.

(28) Li, W. T.; Charters, R. B.; Luther-Davies, B.; Mar, L. *Appl. Surf. Sci.* **2004**, *233* (1−4), 227−233.

(29) Zhang, Y.; Liu, Q.; Xu, B. *Extreme Mech. Lett.* **2017**, *16*, 33−40.

(30) Valentine, J.; Zhang, S.; Zentgraf, T.; Ulin-Avila, E.; Genov, D. A.; Bartal, G.; Zhang, X. *Nature* **2008**, *455* (7211), 376−U32.

(31) Zhang, S. A.; Fan, W. J.; Panoiu, N. C.; Malloy, K. J.; Osgood, R. M.; Brueck, S. R. J. *Opt. Express* **2006**, *14* (15), 6778−6787.

(32) Zhang, S.; Fan, W. J.; Malloy, K. J.; Brueck, S. R. J.; Panoiu, N. C.; Osgood, R. M. *Opt. Express* **2005**, *13* (13), 4922−4930.

(33) Zhao, Y.; Belkin, M. A.; Alu, A. *Nat. Commun.* **2012**, *3*, 870.

(34) Liu, X. L.; Tyler, T.; Starr, T.; Starr, A. F.; Jokerst, N. M.; Padilla, W. J. *Phys. Rev. Lett.* **2011**, *107* (4), 045901.

(35) Goldflam, M. D.; Hawkins, S. D.; Parameswaran, S.; Tauke-Pedretti, A.; Warne, L. K.; Peters, D. W.; Campione, S.; Coon, W. T.; Keeler, G. A.; Shaner, E. A.; Wendt, J. R.; Kadlec, E. A.; Fortune, T. R.; Klem, J. F.; Davids, P. S.; Kim, J. K. In *Next-Generation Infrared Focal Plane Arrays for High-Responsivity Low-Noise Applications*; IEEE Aerospace Conference, Big Sky, MT, Mar 04−11, 2017..

(36) Lee, S. J.; Ku, Z. Y.; Barve, A.; Montoya, J.; Jang, W. Y.; Brueck, S. R. J.; Sundaram, M.; Reisinger, A.; Krishna, S.; Noh, S. K. *Nat. Commun.* **2011**, *2*, 286.

(37) Ku, Z.; Jang, W. Y.; Zhou, J. F.; Kim, J. O.; Barve, A. V.; Silva, S.; Krishna, S.; Brueck, S. R. J.; Nelson, R.; Urbas, A.; Kang, S.; Lee, S. J. *Opt. Express* **2013**, *21* (4), 4709−4716.

(38) Rosenberg, J.; Shenoi, R. V.; Vandervelde, T. E.; Krishna, S.; Painter, O. *Appl. Phys. Lett.* **2009**, *95* (16), 161101.

DOI: 10.1021/acs.nanolett.9b02598
Nano Lett. XXXX, XXX, XXX−XXX

(39) Chang, C. C.; Sharma, Y. D.; Kim, Y. S.; Bur, J. A.; Shenoi, R. V.; Krishna, S.; Huang, D. H.; Lin, S. Y. *Nano Lett.* **2010**, *10* (5), 1704−1709.
(40) Li, Q.; Li, Z. F.; Li, N.; Chen, X. S.; Chen, P. P.; Shen, X. C.; Lu, W. *Sci. Rep.* **2014**.
(41) Huang, E. K. W.; Haddadi, A.; Chen, G. X.; Nguyen, B. M.; Hoang, A.; McClintock, R.; Stegall, M.; Razeghi, M. *Opt. Lett.* **2011**, *36* (13), 2560−2562.
(42) Huang, E. K. W.; Hoang, M. A.; Chen, G. X.; Ramezani-Darvish, S.; Haddadi, A.; Razeghi, M. *Opt. Lett.* **2012**, *37* (22), 4744−4746.
(43) Montoya, J. A.; Tian, Z. B.; Krishna, S.; Padilla, W. J. *Opt. Express* **2017**, *25* (19), 23343−23355.
(44) Fan, W. J.; Zhang, S.; Minhas, B.; Malloy, K. J.; Brueck, S. R. J. *Phys. Rev. Lett.* **2005**.
(45) Fan, W. J.; Zhang, S.; Malloy, K. J.; Brueck, S. R. J. *Opt. Express* **2005**, *13* (12), 4406−4413.
(46) Xu, S.; Yan, Z.; Jang, K.; Huang, W.; Fu, H.; Kim, J.; Wei, Z.; Flavin, M.; McCracken, J.; Wang, R.; Badea, A.; Liu, Y.; Xiao, D.; Zhou, G.; Lee, J.; Chung, H.; Cheng, H.; Ren, W.; Banks, A.; Li, X.; Paik, U.; Nuzzo, R.; Huang, Y.; Zhang, Y.; Rogers, J. *Science* **2015**, *347* (6218), 154−159.
(47) Zhang, Y. H.; Zhang, F.; Yan, Z.; Ma, Q.; Li, X. L.; Huang, Y. G.; Rogers, J. A. *Nat. Rev. Mater.* **2017**, *2* (4), 17019.
(48) Yan, Z.; Zhang, F.; Wang, J. C.; Liu, F.; Guo, X. L.; Nan, K. W.; Lin, Q.; Gao, M. Y.; Xiao, D. Q.; Shi, Y.; Qiu, Y. T.; Luan, H. W.; Kim, J. H.; Wang, Y. Q.; Luo, H. Y.; Han, M. D.; Huang, Y. G.; Zhang, Y. H.; Rogers, J. A. *Adv. Funct. Mater.* **2016**, *26* (16), 2629−2639.
(49) Fu, H. R.; Nan, K. W.; Bai, W. B.; Huang, W.; Bai, K.; Lu, L. Y.; Zhou, C. Q.; Liu, Y. P.; Liu, F.; Wang, J. T.; Han, M. D.; Yan, Z.; Luan, H. W.; Zhang, Y. J.; Zhang, Y. T.; Zhao, J. N.; Cheng, X.; Li, M. Y.; Lee, J. W.; Liu, Y.; Fang, D. N.; Li, X. L.; Huang, Y. G.; Zhang, Y. H.; Rogers, J. A. *Nat. Mater.* **2018**, *17* (3), 268.
(50) Yan, Z.; Han, M. D.; Shi, Y.; Badea, A.; Yang, Y. Y.; Kulkarni, A.; Hanson, E.; Kandel, M. E.; Wen, X. W.; Zhang, F.; Luo, Y. Y.; Lin, Q.; Zhang, H.; Guo, X. G.; Huang, Y. M.; Nan, K. W.; Jia, S.; Oraham, A. W.; Mevis, M. B.; Lim, J. M.; Guo, X. L.; Gao, M. Y.; Ryu, W.; Yu, K. J.; Nicolau, B. G.; Petronico, A.; Rubakhin, S. S.; Lou, J.; Ajayan, P. M.; Thornton, K.; Popescu, G.; Fang, D. N.; Sweedler, J. V.; Braun, P. V.; Zhang, H. X.; Nuzzo, R. G.; Huang, Y. G.; Zhang, Y. H.; Rogers, J. A. *Proc. Natl. Acad. Sci. U. S. A.* **2017**, *114* (45), E9455−E9464.
(51) Wie, D. S.; Zhang, Y.; Kim, M. K.; Kim, B.; Park, S.; Kim, Y. J.; Irazoqui, P. P.; Zheng, X. L.; Xu, B. X.; Lee, C. H. *Proc. Natl. Acad. Sci. U. S. A.* **2018**, *115* (31), E7236−E7244.
(52) Zhang, Y.; Kim, B.; Gao, Y.; Wie, D. S.; Lee, C. H.; Xu, B. *Int. J. Solids Struct.* **2019**, DOI: 10.1016/j.ijsolstr.2019.07.011.

DOI: 10.1021/acs.nanolett.9b02598
Nano Lett. XXXX, XXX, XXX−XXX